Article

Spin-torque skyrmion resonance in a frustrated magnet

Nirel Bernstein [1], Hang Li[2,3], Benjamin Assouline [1], Yong-Chang Lau[3,4], Igor Rozhansky [1,5], Wenhong Wang[2] & Amir Capua [1] ✉

The frustrated Fe_3Sn_2 magnet is technologically attractive due to its extreme-temperature skyrmion stability, large topological Hall effect, and current-induced helicity switching attributed to a self-induced spin-torque. Here, we present a current-driven skyrmion resonance technique excited by self-induced spin-torque in Fe_3Sn_2. The dynamics are probed optically in a time-resolved measurement enabling us to distinguish between the excited modes. We find that only the breathing and rotational counterclockwise modes are excited, rather than the three modes typically observed in Dzyaloshinskii-Moriya interaction-dominated magnetic textures. When a DC current is passed through the crystal, the skyrmion resonance linewidth is modulated. Our micromagnetic simulations indicate that the linewidth broadening arises from an effective damping-like spin-orbit torque. Accordingly, we extract an effective spin Hall conductivity of $\sim 793 \pm 176\,(\hbar/e)\,(\Omega\,cm)^{-1}$. Complementary planar Hall measurements suggest a small yet finite contribution of the real-space spin texture in the electronic transport in addition to a primary k-space contribution. Our results bring new insights into the anisotropic nature of spin-torques in frustrated magnets and to the possibility of using the skyrmion resonance as a sensor for spin currents.

Magnetic skyrmions are attractive candidates for dense data distribution and storage applications. Conventionally, Dzyaloshinskii-Moriya interaction (DMI) is responsible for the skyrmion's topological protection. Recently, it was predicted that also magnetic frustration in ferromagnetic (FM) crystals can provide the topological protection of the skyrmion instead of DMI[1–4] and the effect was soon discovered in Fe_3Sn_2 bulk crystals[5–8]. Fe_3Sn_2 is a technologically promising material system that serves as an excellent platform for exploring the role of spin chirality. The interplay between the exchange interaction, uniaxial magnetic anisotropy (UMA), and dipole-dipole interactions gives rise to a variety of spin configurations including stripes, bubbles, and skyrmions that have displayed extreme thermal stability of up to $\sim 600\,K$[3–5]. Interestingly, the electronic charge transport in Fe_3Sn_2 is strongly affected by the topologies of the band structure and of the real-space spin texture. This is seen by the pronounced topological[9,10]

and anomalous Hall effects (THE and AHE, respectively)[11,12]. Furthermore, recent experiments showed that electrical currents can drive the motion of skyrmions in Fe_3Sn_2 and even switch their helicity and topological charge Q[7,13,14]. The switching effect was attributed to a self-induced spin-torque that is assisted by Joule heating[3,14], yet the underlying mechanism is still debated.

Current-driven dynamics of skyrmions in bulk crystals are usually excited through spin-transfer torques (STT) by spin-polarized electric currents that interact with the localized spins[15]. However, Fe_3Sn_2 exhibits a unique combination of a layered kagome crystal structure with magnetic frustration and a non-vanishing spin-orbit coupling (SOC) which may give rise to an additional spin-orbit torque (SOT). SOC is well known to affect the k-space band topology leading to the spin Hall effect (SHE)[16,17]. Additionally, in layered materials, vertical spin currents can arise from interfacial spin-orbit interactions. Often,

[1]Institute of Applied Physics, The Hebrew University of Jerusalem, Jerusalem, Israel. [2]School of Electronics and Information Engineering, Tiangong University, Tianjin, China. [3]Beijing National Laboratory for Condensed Matter Physics, Institute of Physics, Chinese Academy of Sciences, Beijing, China. [4]University of Chinese Academy of Sciences, Beijing, China. [5]National Graphene Institute, University of Manchester, Manchester, UK. ✉e-mail: amir.capua@mail.huji.ac.il

the role of SOC in determining the band topology can be substituted by the spin chirality of the magnetic texture[18]. This is the origin of the momentum (k) space contribution to the THE where the Berry phase in momentum space is produced by the spin chirality of the localized spin structures such as skyrmions[19–21]. Alternatively, the real-space magnetic topology of the localized spin structures can also cause the THE. The underlying microscopic mechanism of the real-space spin texture contribution to the THE was described by spin separation which arises from the opposite polarity of the emergent magnetic field for opposite spins[21–24]. Therefore, in addition to the transverse charge current that arises when spin populations are uneven, e.g., as in FMs, this was also predicted to result in a spin current[22,24–26]. Figure 1a schematically illustrates these spin and charge transport phenomena. The multitude of mechanisms capable of generating spin-torque highlights the technological relevance of Fe_3Sn_2 while also posing a major challenge in unlocking its full potential.

Microwave resonance experiments are pivotal for probing spin-torques. However, in textured magnets, the Slonczewski spin-torque becomes highly anisotropic rendering its effect unclear. Furthermore, the complexity is aggravated by the relatively less explored nature of skyrmion resonance dynamics. Early theoretical studies of the skyrmion resonance dynamics predicted the excitation of two fundamental in-plane (IP) rotational clockwise (CW) and counter-clockwise (CCW) modes and a third out-of-plane (OOP) breathing mode[27]. These modes were measured immediately afterwards in a cubic helimagnet[28]. In the cubic metallic, semiconducting, and insulating chiral magnets such as MnSi, $Fe_{1-x}Co_xSi$, and Cu_2OSeO_3, respectively, it was shown that the dynamics of magnetic textures follow universal laws determined solely by the chiral and critical field energies[29]. In contrast, the strong UMA in the rhombohedral GaV_4S_8 chiral magnet was shown to interchange the hierarchy of the excitations[30]. The UMA was also responsible for annihilating the CW mode in multilayered thin films where the skyrmions are stabilized by interfacial DMI and UMA[31,32]. Interestingly, in frustrated triangular magnets, it has been predicted that UMA can strongly influence the spin ordering, leading to a complex resonance spectrum that is accompanied by oscillations of the electric polarization[1]. The complexity of the dynamics was attributed to the nonlinear coupling between the additional helicity degree of freedom present in frustration-induced magnetic skyrmions and the skyrmion's center of mass. Furthermore, the study also predicted that only the CW and breathing modes can be excited in such a system. Despite the significant physical insights that can be captured by studying the skyrmion resonance in frustrated magnets, the empirical validation of the predicted dynamics remains very limited.

Primarily, the skyrmion resonance dynamics were explored using broadband microwave absorption spectroscopy[28–32]. However, it is well known that the ferromagnetic resonance (FMR) can also be excited by AC spin-torques. This is known as the spin-torque FMR (STFMR) which proved highly effective for exploring SOTs[33]. To this end, a FM is deposited on the material of interest and serves as a spin current sensor by measuring the current-induced FMR linewidth modulation. However, in textured magnets, the additional FM is bound to suppress the texture, potentially eliminating it, and as a result deform the topologies of both the energy bands and of the spin texture in k- and real-spaces, respectively.

Here, we report a time-resolved optically probed spin-torque driven skyrmion resonance technique in which the dynamics are excited by a self-induced RF spin-torque in a fashion that is reminiscent of the STFMR technique[33]. We apply the technique to the frustrated Fe_3Sn_2 crystal and find that indeed only the breathing and CCW skyrmion modes are excited in accord with theoretical predictions. The dynamical responses illustrate the magnetic phase transitions from a disordered state to a stripe phase and finally to an ordered lattice phase as the externally applied magnetic field is increased. Interestingly, when a DC charge current is passed through the crystal, we

observe that the linewidth of each mode is modulated depending on the magnetic phase. Micromagnetic time-domain numerical simulations that account for the STT and SOT indicate that while the AC STT and AC SOT are both capable of exciting the skyrmion resonance dynamics, only the DC SOT is capable of modulating the linewidth. Complementary transport measurements reveal a primary k-space and a small yet finite real-space contribution to the Hall and planar Hall effects (PHE) highlighting a possible connection between the spin texture and the damping-like torque. The experimental technique is thus key for the understanding of spin dynamics in textured magnets and for developing relevant applications in frustrated magnets.

Results

The Fe_3Sn_2 crystal has a rhombohedral unit cell which belongs to the $R\bar{3}m$ space group. It consists of alternating double kagome Fe-Sn and hexagonal Sn layers stacked along the c-axis (Fig. 1b) having lattice constants of $a = b = 5.338$ Å and $c = 19.789$ Å in hexagonal coordinate system[34]. The adjacent kagome Fe-Sn layers are offset, and each consists of two different Fe-Fe bond lengths of 2.732 Å and 2.582 Å. Crystals of Fe_3Sn_2 were synthesized by chemical vapor transport reaction as described in 'Methods'. Figure 1c presents a scanning electron microscope (SEM) image of the crystal.

The magnetization dynamics were studied using an optically probed STFMR technique (OSTFMR)[33,35,36]. An RF charge current of frequency f was passed through the crystal and excited the dynamics. The responses were probed using a femtosecond laser that was phase-locked to the RF signal. The OOP component of the RF magnetization, m_z, was probed using the magneto-optical Kerr effect (MOKE) and an optical delay line provided the temporal resolution. The current was passed along the $\hat{x}$ direction corresponding to the [100] crystal axis and the external magnet field $\vec{H}$ of magnitude H_0 was applied in the sample plane at $\theta_H = 30°$ with respect to the [100] axis as indicated in Fig. 1c (see 'Methods' for further details).

An example of an OSTFMR trace at 14 GHz is presented in Fig. 1d. The trace presents $m_z(t)$ as a function of H_0 in which a resonance peak appears at ~ 300 mT. The extracted phase response, $\phi(H_0)$, is represented by the black dashed line. Interestingly, $\phi(H_0)$ reveals a total phase shift, $\Delta\phi$, of $\sim 2\pi$ accumulated across the resonance rather than the expected π shift, indicating that actually two resonance modes were measured. This is confirmed by plotting the amplitude response $|m_z(H_0)|$ presented in Fig. 1e that reveals a secondary feature at ~ 250 mT. Namely, the AC magnetic susceptibility consists of two Lorentzian lines $\chi_m = \sum_{i=1,2} A_i \cdot \frac{1}{\left(H_{res_i}^2 - H_0^2\right) + iH_0\Delta H_i} \cdot e^{i\phi_i}$ where A_i, H_{res_i}, and ΔH_i are the amplitude, resonance field, and linewidth of each resonance mode, and ϕ_i is the phase relative to the RF excitation. The reconstructed $m_z(H_0)$ is presented as well in Fig. 1e together with the two retrieved modes and agrees well with the measurement. Using micromagnetic simulations that account for the exchange, dipole-dipole, tilted UMA, and Zeeman energies (see 'Methods'), we find that the lower (higher) resonance field corresponds to the CCW (breathing) mode. In the general case, the CW mode should also be excited, however, it is typically of a smaller amplitude while the combined effect of frustration and strong exchange interaction further suppress its excitation[1]. The driving RF torque can stem from the RF Oersted or RF spin-torque. In frustrated magnets, an IP RF Oersted field can only drive the CCW mode[1,27]. In contrast, the RF spin-torque consists of IP and OOP components that can excite also the translational mode. Namely, the excitation of the two orthogonal modes implies the generation of RF spin-torque in the crystal. The negligible self-induced Oersted torque[33] was verified by passing a DC current density $\vec{J}_c$ of magnitude J_c which had no effect on H_{res_i} as seen in Fig. 1f.

The same analysis was repeated for additional frequencies. The top panels of Fig. 2a show characteristic spectra measured at 6, 8, 12,
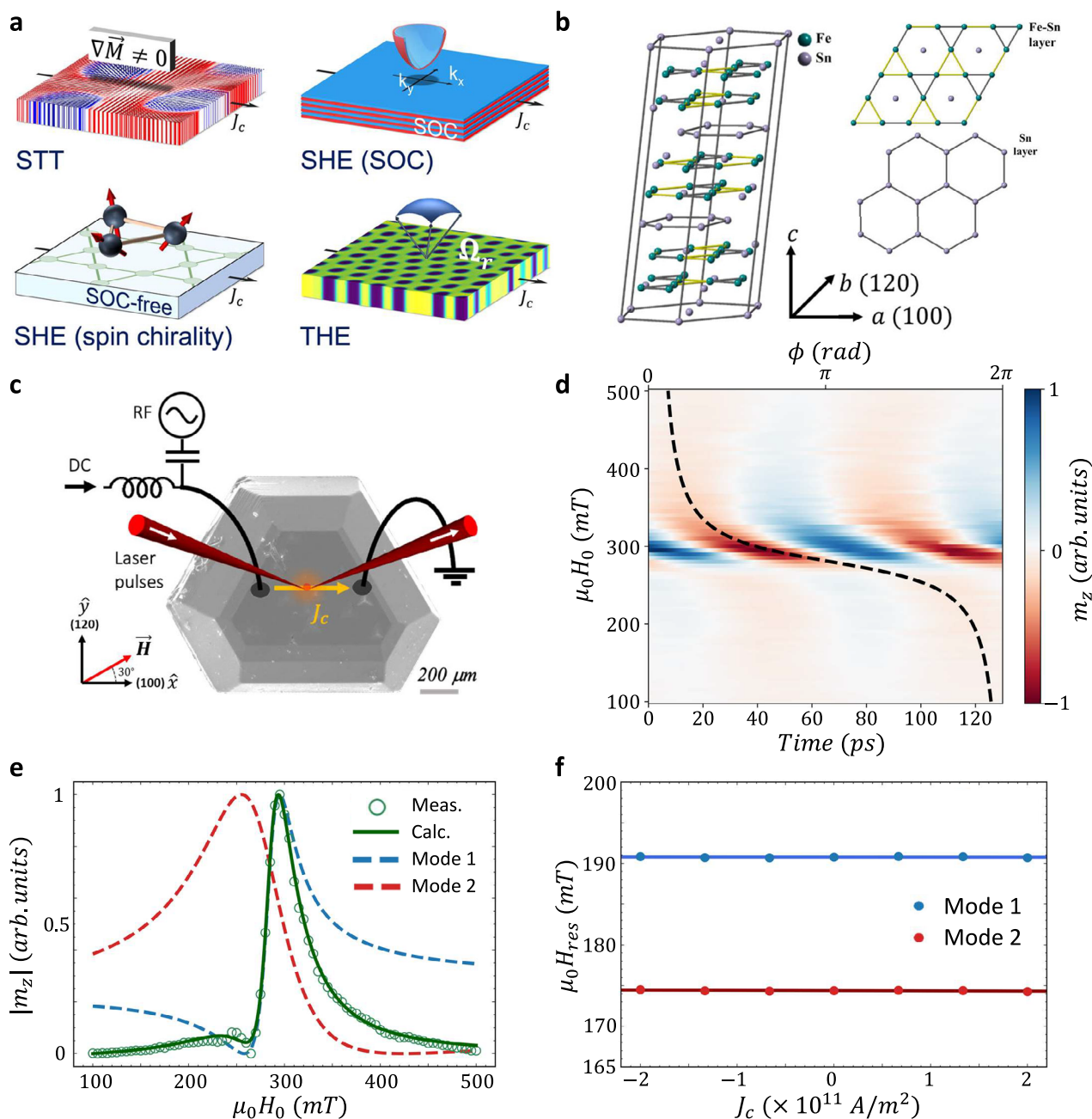
Fig. 1 | Characteristic OSTFMR measurement. a Schematic illustration of charge and spin transport mechanisms in Fe_3Sn_2: spin-polarized electric currents responsible for STT, SOC-based bulk and interfacial SHE, THE induced by k-space band topology emerging from spin-chirality, and THE induced by real-space topology of localized spin structures. **b** Crystal structure of Fe_3Sn_2. **c** SEM image of the Fe_3Sn_2 crystal together with a schematic of the experimental technique. RF currents are driven through the crystal and excite the skyrmion resonance. m_z is detected in a polar-MOKE configuration using a phase-locked femtosecond laser. **d** OSTFMR trace of $m_z(t, H_0)$ at $14\,GHz$. Black dashed line indicates ϕ vs. H_0. **e** Measured amplitude response $|m_z(H_0)|$ (green open circles) together with the two fitted modes (red and blue dashed lines) and the reconstructed response (green solid line). **f** Extracted H_{res} at $10\,GHz$ for different values of J_c. J_c was estimated using the Poisson equation while accounting for the geometrical dimensions of the crystal (details in Supplementary Note 2). In (**d**, **e**) m_z was normalized to its peak value.

and $14\,GHz$. At high frequencies, distinct resonances appear whereas at low frequencies the spectrum is random. This behavior is summarized by plotting the $f - H_{res_i}$ dispersion relations presented in the main panel of the figure. A phase transition is seen at $\sim 10\,GHz$ ($\sim 175\,mT$). This transition can be understood from the dynamical micromagnetic simulations. To this end, the static textures were first determined and are presented in the top panels of Fig. 2b. A disordered phase is seen at $H_0 = 0$ that evolves into a stripe phase at $75\,mT$ after which an ordered lattice phase emerges. When H_0 is further increased, the texture gradually saturates. The dynamical responses were obtained from the Fourier transform of the impulse response of the mean OOP magnetization M_z and are presented in the main panel of Fig. 2b. The calculated dynamics correlate with the magnetic phase transitions and reproduce the trends seen in the measurements: scattered resonance peaks measured at $\mu_0H_0 < 150\,mT$ and a homogeneous monotonic dispersion curve consisting of two modes at high H_0. Indications of the stripe phase are also found in the measurement as seen in the spectrum of $8\,GHz$ which is significantly broader due to the higher
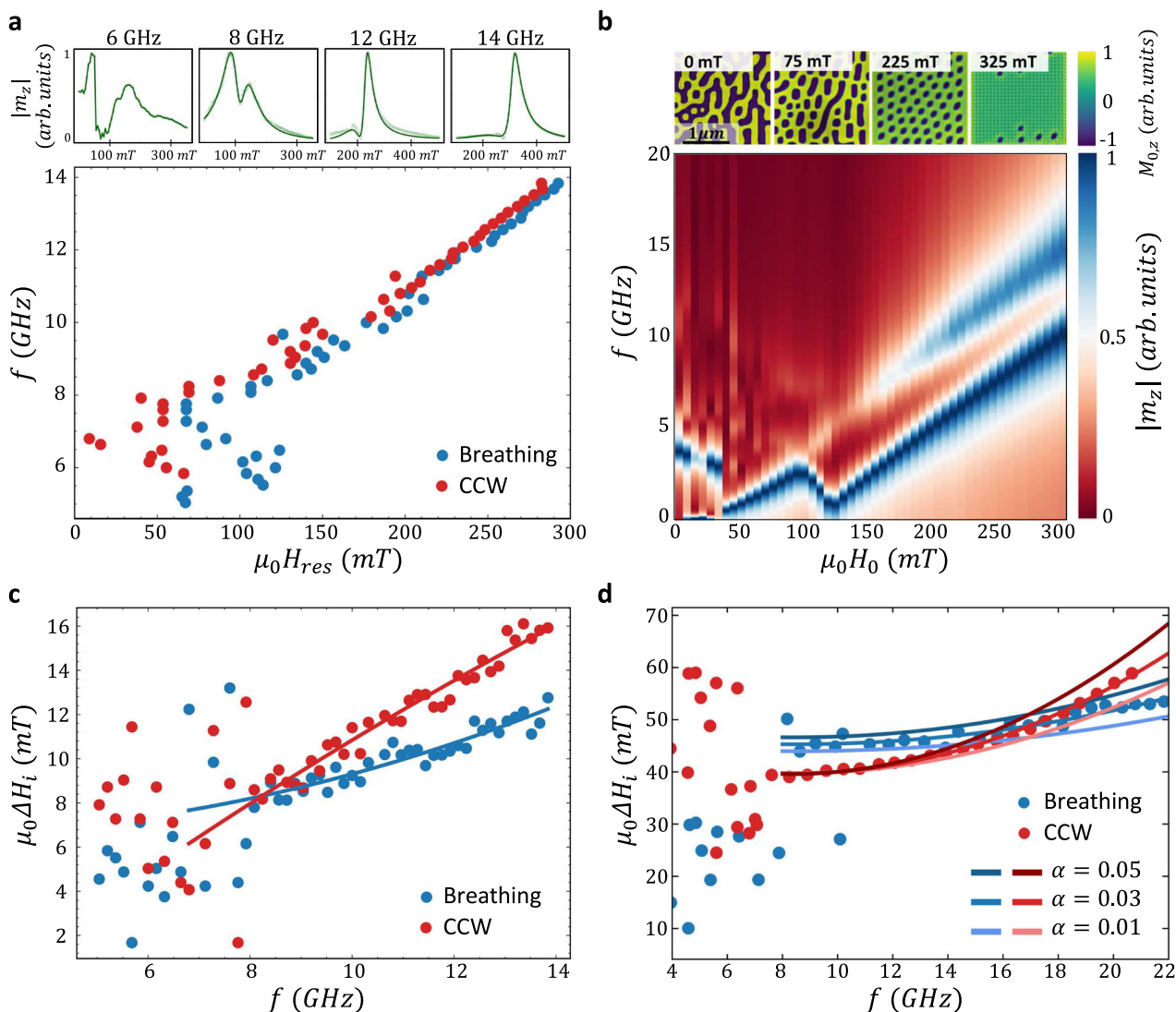
Fig. 2 | Measured and calculated resonance dynamics of Fe₃Sn₂. a Measured dynamical response. Top panels present measured $|m_z|$ as a function of H_0 at 6, 8, 12, and 14 GHz (light green open circles). Reconstructed responses are indicated in green solid line. Data is presented in normalized units. Main panel: Frequency dispersion relations of the breathing and CCW resonance modes. **b** Micromagnetic dynamical simulations. Top panels present the calculated textures at $\mu_0 H_0 = 0$, 75, 225, and 325 mT. The textures are represented by plotting the equilibrium OOP component of the magnetization, $M_{0,z}$. The main panel presents the calculated frequency response of $|m_z|$ as a function of H_0 for $\alpha = 0.05$. Each response was normalized to its peak value. **c** Measured resonance linewidths (ΔH_i) of CCW and breathing modes as a function of f. Solid lines represent a fit to a second order polynomial function. **d** Calculated ΔH_i of the two modes. Solid lines illustrate the calculation for $\alpha = 0.01$, 0.03, and 0.05. In (**a**, **c**, **d**) data of the breathing and CCW modes are indicated by blue and red colors, respectively.

motional degrees of freedom. From the calculations, $Q = 0$ was determined in the lattice phase (see Supplementary Note 3). Following the conventional terminology, we use the term skyrmion resonance although the magnetic texture is topologically trivial.

Interestingly, features appearing in the measured resonance linewidths are also reproduced in the calculation. Figure 2c presents the measured ΔH_i as a function of f. It is seen that ΔH of the CCW mode increases more rapidly with f as compared to the breathing mode. The same behavior is seen in the calculated ΔH_i presented in Fig. 2d which was obtained using $\Delta H_i = \left(\frac{\partial f_{res}}{\partial H_0}\right)^{-1} \Delta f_i$. The overall broader calculated ΔH_i stems from the inhomogeneous broadening induced by the interfaces of the finite calculation space. A Gilbert damping of $\alpha = 0.032 \pm 0.008$ was evaluated from the f dependent ΔH broadening of the CCW mode in the range $f > 10$ GHz which is comparable to previously measured values in thin films of Fe₃Sn₂[37]. In the CCW mode, the spins undergo a local precessional trajectory about an effective field. Therefore, the Rayleigh viscous-like damping process

manifests in the measured quasi-linear dependence at high f. In contrast, in the breathing mode, the spins follow a non-conical expansion and contraction-type motion that results in a weaker dependence of ΔH on f.

Next, we examine the influence of J_c on the skyrmion resonance linewidth. In the following experiments, the current was passed along the [100] axis. Figure 3a–c present the measured data for the disordered, stripe, and lattice phases by plotting the variation of ΔH_i relative to the zero-bias linewidth ΔH_i^0. In the disordered phase, a significant random modulation of $\Delta H_{1,2}$ appears which stems from switching of the textures by J_c[7]. In the stripe and lattice phases, ΔH_1 increases monotonically with J_c while ΔH_2 decreases. In FMR measurements of a non-textured saturated magnetization, the linewidth is directly related to the magnetic losses, therefore, a current induced linewidth broadening is indicative of a damping-like torque. However, in textured magnets, the relation between the Slonczewski damping-like torque and resonance linewidth is not straight forward due to the
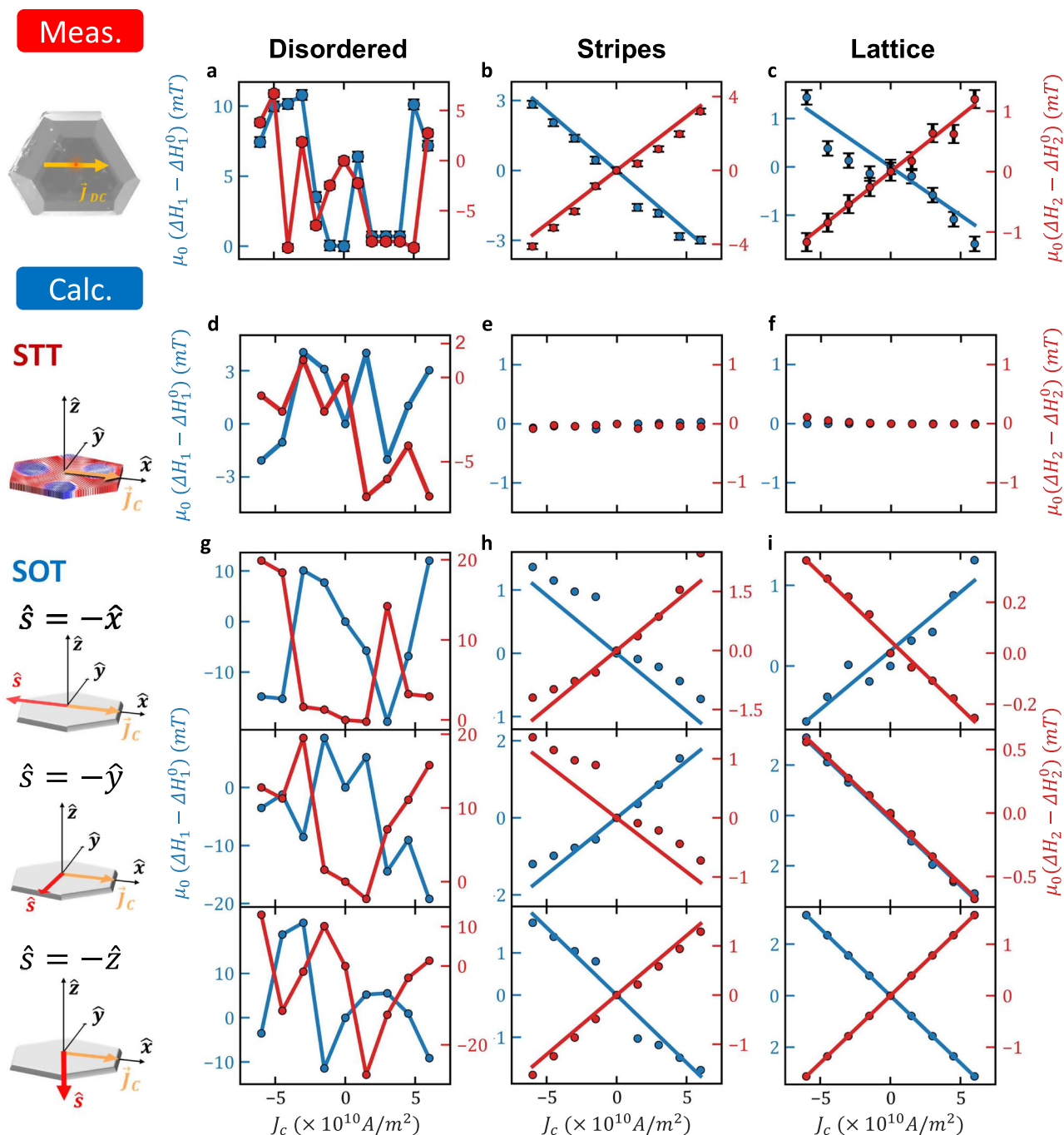
Fig. 3 | Measured and calculated current induced skyrmion resonance linewidth broadening at the disordered, stripe, and bubble lattice phases.
a–**c** Measured $\Delta H_i - \Delta H_i^0$ at 5, 10, and 12 GHz. **d**–**f** Calculated $\Delta H_i - \Delta H_i^0$ for DC STT. **g**–**i** Calculated $\Delta H_i - \Delta H_i^0$ for DC SOT. The figures present the calculation for $\hat{s} = -\hat{x}, \hat{s} = -\hat{y}$, and $\hat{s} = -\hat{z}$. In the simulations, ΔH_i for the disordered, stripe, and lattice phases were calculated at $\mu_0 H_0 = 10$, 100, and $250\,mT$, respectively, corresponding to the measurements at 5, 10, and 12 GHz. Left, middle, and right columns correspond to the disordered, stripe, and bubble lattice phase, respectively. Red and blue solid lines correspond to the CCW and breathing modes, respectively.

anisotropic nature of the torque. To elucidate this behavior, the torque was included in the micromagnetic simulations by introducing STT and SOT terms of the forms $\tau_{STT}\hat{m} \times \hat{m} \times (\vec{J_c}\nabla)\hat{m}$ and $\tau_{SOT}J_c\hat{m} \times \hat{m} \times \hat{s}$, respectively. Here, τ_{STT} and τ_{SOT} are coefficients of the two torques and $\hat{s}$ is the spin polarization of the SOT (see 'Methods'). Figure 3d–f present the simulation results for the case of a DC STT by plotting the J_c-dependent ΔH_i. In the disordered phase, a J_c-induced texture switching takes place which manifests in the random modulation of ΔH_i. However, no discernable modulation of the linewidth is observed

in the stripe and lattice phases. This trend persists up to a critical value of J_c after which the texture switches also in these phases (see Supplementary Note 4). In contrast, the application of a DC SOT leads to the modulation of ΔH_i observed experimentally. The SOT case was studied for $\hat{s}$ along the three principal axes as presented in Fig. 3g–i. In the disordered phase, the texture switching is reproduced while a monotonic dependence of ΔH_i on J_c is calculated in the stripe and lattice phases. It is seen that the case of $\hat{s} = -\hat{z}$ best reproduces the measurements. Alternatively, also a combination of $\hat{s} = -\hat{z}$ and $\hat{s} = -\hat{x}$
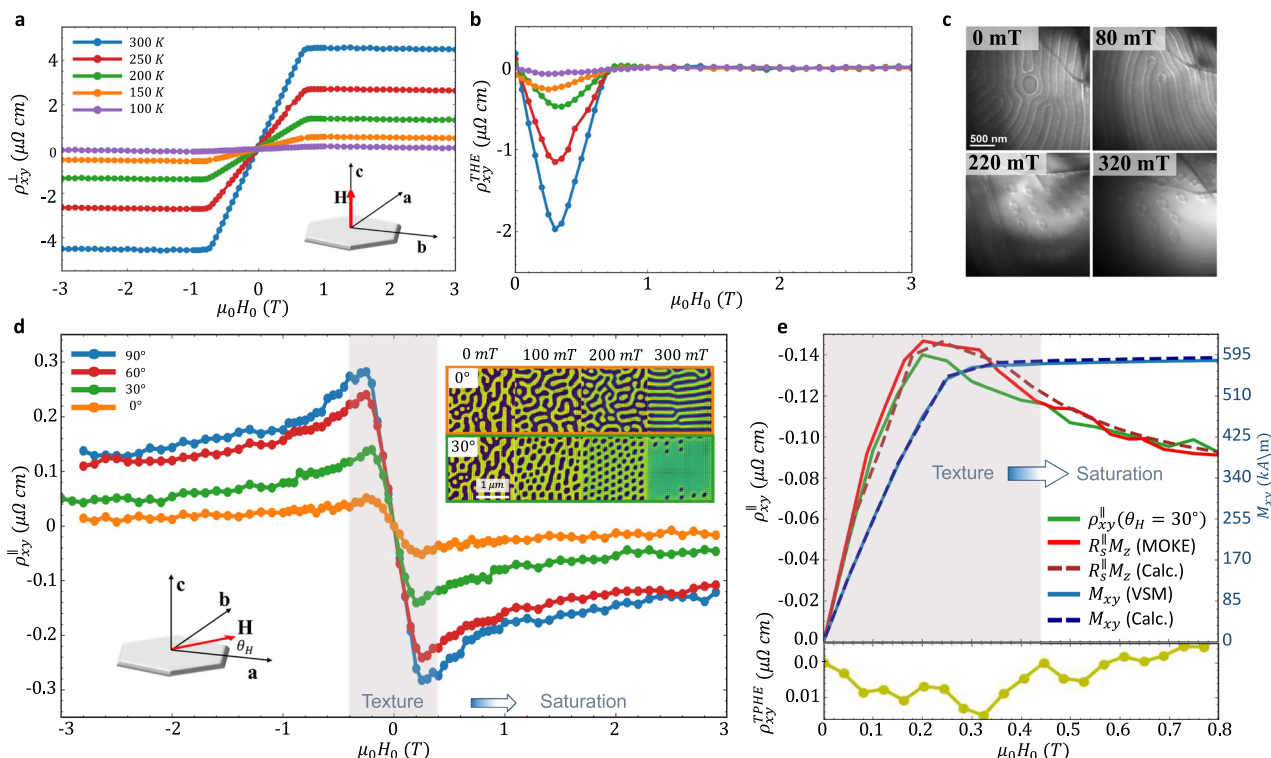
Fig. 4 | Angle and temperature dependent DC Transport measurements.
a Temperature dependence of $\rho_{xy}^{\perp}$ with OOP $\vec{H}$. **b** Temperature dependence of ρ_{xy}^{THE}. ρ_{xy}^{THE} is extracted by subtracting the OHE and AHE contributions from $\rho_{xy}^{\perp}$. **c** LTEM images at 300 K for $\mu_0 H_0 = 0, 80, 220,$ and $320\,mT$ in the OOP configuration. **d** PHE measurements of $\rho_{xy}^{\parallel}$ for IP $\vec{H}$ applied at $\theta_H = 0°, 30°, 60°,$ and $90°$ with respect to the [100] axis. Inset presents calculated magnetic textures for $\theta_H = 0°$ and $30°$. **e** Extraction of the topological contribution, ρ_{xy}^{TPHE}, at $\theta_H = 30°$. Upper panel:

Measurement of $\rho_{xy}^{\parallel}$ (green solid line) together with the measured $R_s^{\parallel} \mu_0 M_z$ (red line) at $\theta_H = 30°$. M_z was measured using a MOKE setup at $\theta_H = 30°$ (red line). $R_s^{\parallel}$ was determined from $\rho_{xy}^{\parallel}$ at the saturated magnetization regime. Saturation conditions were verified by calculating M_z at $\theta_H = 30°$ (red dashed line) and by measuring M_{xy} using a VSM (blue solid line). Calculated M_{xy} (blue dashed line) reproduces the measured M_{xy} in saturation. Lower panel presents the extracted ρ_{xy}^{TPHE}.

may result in a similar trend. In the stripe phase, the inhomogeneous broadening is more significant. Therefore, the effective spin Hall angle was estimated from the CCW mode at the lattice phase for $\hat{s} = -\hat{z}$ which resulted in $\theta_{SH}^{eff} = 0.027 \pm 0.006$ (see 'Methods').

The THE is a useful probe of texture-driven transport phenomena and appears as an anomaly in the AHE response[38,39]. Figure 4a presents temperature dependent Hall resistivity $\rho_{xy}^{\perp}$ which consists of the contributions of the ordinary Hall effect (OHE), AHE, and THE[40]. For high $|H_0|$, M_z is saturated so that the THE vanishes and the AHE dominates. At lower $|H_0|$, the THE arises. This is readily seen in Fig. 4b by plotting the THE contribution, ρ_{xy}^{THE}, obtained by subtracting the contributions of the OHE and AHE (see 'Methods'). ρ_{xy}^{THE} survives up to 700 mT where the maximal value occurs at $\mu_0 H_0 \approx 300\,mT$ and accounts for nearly 50% of $\rho_{xy}^{\perp}$. This highlights the significant role of the real-space Berry curvature in Fe_3Sn_2[9]. Lorentz transmission electron microscopy (LTEM) images presented in Fig. 4c further support this conclusion revealing that a skyrmion lattice forms having $Q \neq 0$ at the maximal value of ρ_{xy}^{THE}.

In contrast to the measurement of the THE, in the OSTFMR measurements $\vec{H}$ was applied in the sample plane. Therefore, the planar Hall resistivity $\rho_{xy}^{\parallel}$ was also measured and is presented in Fig. 4d. In this geometry, the tilted UMA produces a non-vanishing M_z giving rise to the usual AHE that originates in the k-space band topology in addition to the effective magnetic field that emerges from the localized spin structure in real-space. We refer to these contributions as the k-PHE and topological PHE (TPHE) analogously to the AHE and THE terms of $\rho_{xy}^{\perp}$. Accordingly, $\rho_{xy}^{\parallel} = R_s^{\parallel} \mu_0 M_z + P_z^{\parallel}(H_0) R_0^{\parallel} b^z$ where $R_s^{\parallel}$ and $R_0^{\parallel}$ are the k-PHE and TPHE coefficients, respectively, $P_z^{\parallel}(H_0)$ is the net $\hat{z}$ spin polarization of the charge carriers, and b^z is the fictitious gauge field emerging from

the real-space Berry curvature. $P_z^{\parallel}(H_0) = C_0 \cdot |M_z/M_s|$ with the constant C_0 determined by the material band structure and M_s is the saturation magnetization. The figure presents $\rho_{xy}^{\parallel}$ for different IP θ_H angles together with the calculated magnetic textures at $\theta_H = 0°$ and $30°$ (textures for $\theta_H = 60°, 90°$ are presented in Supplementary Note 5). $\rho_{xy}^{\parallel}$ is substantially smaller than $\rho_{xy}^{\perp}$ due to the smaller M_z and $P_z^{\parallel}$ in the planar geometry. The non-monotonic behavior of $\rho_{xy}^{\parallel}$ is a hallmark of the formation of a multi-domain texture in PHE measurements[41]. For $\theta_H = 30°$ at which the OSTFMR measurements were carried out, the maximal value of $\rho_{xy}^{\parallel}$ occurs at 198 mT corresponding to the bubble lattice phase. At $\theta_H = 0°$, the simulations reveal that the lattice phase does not form, therefore, $\rho_{xy}^{\parallel}$ should not exhibit a peak. Indeed, the measured $\rho_{xy}^{\parallel}$ is smaller as compared to the case of $\theta_H = 30°$, however, a slight peak is still observed and stems from a slight misalignment of $\vec{H}$ as verified in Supplementary Note 6. At $\theta_H = 30°$ and $|\mu_0 H_0| > 400\,mT$, the texture saturates resulting in $b^z \approx 0$ and the response purely stems from the k-space PHE. In the presence of the tilted UMA axis, M_z saturates to different values depending on θ_H. Consequently, $\rho_{xy}^{\parallel}$ approaches a different limit as θ_H is varied. The different saturation limits were also verified in the calculation (see Supplementary Note 6).

To determine the TPHE contribution at $\theta_H = 30°$, M_z was measured using a static MOKE. This data is presented in Fig. 4e (red solid line) together with the measured $\rho_{xy}^{\parallel}(\theta_H = 30°)$ (green solid line). M_z is represented by plotting $R_s^{\parallel} \mu_0 M_z$ where $R_s^{\parallel}$ was determined from the saturated $\rho_{xy}^{\parallel}$ responses at high H_0. The TPHE contribution ρ_{xy}^{TPHE} was extracted by subtracting $R_s^{\parallel} \mu_0 M_z$ from $\rho_{xy}^{\parallel}$ and is plotted in the lower panel of the figure. This procedure was additionally validated by vibrating sample magnetometer (VSM) measurements of the IP magnetization, M_{xy} (blue solid line), and a numerical calculation of M_z and

M_{xy} (red and blue dashed lines, respectively) which reproduced the measurement in the saturation regime. It is seen that $\rho_{xy}^{\parallel}$ primarily stems from the k-space PHE while the maximal contribution of ρ_{xy}^{TPHE} is $\sim 10.7\%$ obtained at $\sim 320\,mT$ and is significantly smaller than the relative contribution of the THE in the measurement of $\rho_{xy}^{\perp}$. Once more, the maximal value of ρ_{xy}^{TPHE} corresponds to a lattice phase as seen from the calculated textures displayed in Fig. 4d. At $250\,mT$ where θ_{SH}^{eff} was extracted, ρ_{xy}^{TPHE} accounts for 8.5% of $\rho_{xy}^{\parallel}$.

Discussion

The PHE transport measurements illustrate that the spin texture plays a small yet finite role in the carrier transport mechanisms. These results suggest a possible contribution of the magnetic texture also to the spin transport. While our simulations imply a negligible effect of the DC STT on the resonance linewidth, the SHE or interfacial spin-orbit interactions may certainly be the dominant mechanisms. The predictions of the possible THE contribution due to the real-space magnetic topology of the localized spin structures is relevant in the adiabatic regime[21–24]. In this regime, the carrier and the scatterer are strongly coupled such that the itinerant electrons follow the direction of the local magnetization and the spin-dependent emergent magnetic field due to the real-space Berry curvature arises[24]. The coupling strength is given by the adiabatic parameter $\lambda = \tau_{fl}/\tau_{ex}$ which represents the ratio between the time of flight through the localized spin texture and the exchange-driven spin-flip time[42]. The exchange splitting energy was estimated to be $\sim 22\,meV$ (see 'Methods'), in agreement with recent measurements[43]. Accordingly, $\tau_{ex} \sim 30\,fs$ was determined. For the spin texture diameter of $100\,nm$ and Fermi velocity $v_F \approx 10^5 - 10^6\,ms^{-1}$ [12,44], τ_{fl} was estimated to be $10^{-12} - 10^{-13}\,s$. Therefore, $\lambda \approx 3 - 30$ indicating an intermediate coupling regime in which the transition from spin-dependent to spin-independent scattering occurs[42]. For the extreme case in which all scattering mechanisms are spin-dependent, the texture dependent and texture independent spin Hall conductivities are $\sim 726 \pm 161\,(\hbar/e)\,(\Omega cm)^{-1}$ and $\sim 67 \pm 15\,(\hbar/e)\,(\Omega cm)^{-1}$, respectively.

In this work, we studied the skyrmion resonance response in a frustrated Fe$_3$Sn$_2$ magnet. The dynamics were excited by a self-induced RF spin-torque rather than an RF Oersted field, while the magnetization response was probed optically in a time-resolved measurement. Our results indicated that only the CCW and breathing modes are excited, confirming the theoretical predictions for frustrated magnets. Although the spin-torque is anisotropic, our experiments revealed that the application of a DC bias current is capable of modulating the resonance linewidth in a fashion that is reminiscent of conventional SHE measurements in which an adjacent FM layer is used as a spin-current sensor. Micromagnetic simulations illustrated that the skyrmion resonance linewidth is sensitive to an SOT-like mechanism rather than a DC STT. In Fe$_3$Sn$_2$, for the given planar geometry, transport measurements suggest a primary k-space contribution to an SOT-type mechanism and a smaller contribution of the real-space spin texture. This is another indication of the generally weaker contribution of the real-space spin texture as compared to the k-space band topology.

These results provide insights into the anisotropic nature of spin-torque in frustrated magnets and advances the possibility of using the skyrmion resonance as a sensor for spin currents. Natural extensions of the work include the search for more pronounced real-space effects anticipated in the strongly adiabatic regime for a topologically non-trivial scatterer. To gain a deeper understanding of the interplay between real-space and momentum-space induced phenomena, it would be valuable to explore a variety of magnetic textures, including trivial and topologically protected states of higher Q. Relevant materials include helimagnets, ferromagnets, additional frustrated magnets, and antiferromagnets. These encompass systems with bulk DMI, interfacial DMI, strong uniaxial magnetic anisotropies (UMA), and defect-engineered structures. Of particular interest are thin film systems that are pivotal to the future applications. A more comprehensive study will contribute in identifying the universal laws that govern the skyrmion resonance dynamics[29] in the presence of spin polarized currents. Having the ability to address the skyrmion dynamics using optical techniques, rather than relying on microwave absorption, provides advantages in sensitivity and offers a more direct, artifact-free approach. The applicability of our approach is expected to have broad ramifications for the control of magnetic textures in a variety of applications including data storage and transfer, neuromorphic and reservoir computing, and magnetic sensing, with advantages in density, power, and scalability.

Methods

Crystal growth

The Fe$_3$Sn$_2$ polycrystalline powder and I$_2$ (mass ratio $10 : 1$) were sealed in vacuum quartz tube which was then placed in a horizontal three-temperature-zone tube furnace with a temperature gradient from $650\,°C$ to $750\,°C$. The raw material was kept at $650\,°C$ for ~ 150 hours and then quenched into cold water. The resultant crystal dimensions were roughly $\sim 0.85 \times 1\,mm^2$ and $55\,\mu m$ thick having resistivity of $\rho_{xx} = 68.1\,\mu\Omega \cdot cm$. X-ray diffraction data revealed a hexagonal surface in the (001) plane (see Supplementary Note 1).

OSTFMR technique

The dynamics were probed using a Ti:Sapphire laser emitting $35\,fs$ pulses at $800\,nm$ and a repetition rate of $80\,MHz$. The laser was focused to a probing spot size of $\sim 10\,\mu m$. J_c was estimated from the Poisson equation while accounting for the geometrical dimensions of the crystal (see Supplementary Note 2).

Micromagnetic simulations

Micromagnetic simulations were performed using object oriented micromagnetic framework (OOMMF)[45] taking the energy density:
$$E_T = -A\vec{m} \cdot \nabla^2 \vec{m} - \frac{1}{2}\mu_0 M_s \vec{m} \cdot \vec{H}_d - K(\vec{m} \cdot \hat{u})^2 - \mu_0 M_s \vec{m} \cdot \vec{H},$$
where $M_s = 566\,kA/m$, and the exchange stiffness and anisotropy constants were $A = 2 \cdot 10^{-11}\,J/m$ and $K = 1.8 \cdot 10^5\,J/m^3$, respectively. $\hat{u}$ is the unit vector of the anisotropy axis which was tilted at $22°$ from the OOP axis along $\hat{x}$[5,9]. $\vec{H}_d$ is the demagnetization field and was evaluated numerically. The exchange length under these parameters is $\sqrt{A/0.5\mu_0 M_s^2} = 9.97\,nm$. The calculation space was $2 \times 2\,\mu m^2$ and $100\,nm$ thick and was discretized into $5 \times 5 \times 5\,nm^3$ unit cells. The initial state was determined by initializing each unit cell to a random value after which the magnetization relaxed to its ground state. The frequency response was obtained by taking the Fourier transform of the calculated impulse response at a constant H_0.

STT modeling

The STT was incorporated into the micromagnetic simulations by including the Zhang-Li term[46], $-\frac{1+\alpha\beta}{1+\alpha^2}\hat{m} \times (\hat{m} \times (\vec{u} \cdot \nabla)\hat{m})$, where the non-adiabatic coefficient β was set to 0.1 as in ref. [47]. The Zhang-Li coefficient is given by $\vec{u} = \frac{J_c P \mu_B}{e M_s}$ for which μ_B is the Bohr magneton, e is the elementary charge. The polarization rate was set to $P = 1$ to estimate the upper limit of the STT. The linewidth was calculated from the Fourier transform of the impulse response.

SOT modeling and extraction of θ_{SH}^{eff}

The generation of spin currents within the calculated volume was modeled assuming an average spin-flip length of λ_{flip} in which the spin polarized electrons transfer their spin angular momentum. This torque was modeled by introducing the Slonczewski spin-torque $-\gamma \frac{1}{\mu_0 M_s} \frac{\hbar}{2e} \frac{J_c}{\lambda_{flip}} \theta_{SH}^{eff} (\hat{m} \times \hat{m} \times \hat{s})$ which was injected into each discretized

cell. Here, $\theta_{SH}^{eff} = J_s/J_c$ with J_s being the spin current density and $\hbar$ is the reduced Planck's constant. λ_{flip} determined the cell size. The inter-cell propagation of spin angular momentum was set to zero. A λ_{flip} of $5\,nm$ was estimated from the Fermi velocity and the exchange driven spin flip time by $v_F \cdot \tau_{ex}$ using typical values in FMs[48].

Lorentz TEM

The LTEM measurements were performed by Tecnai F20 in the Lorentz mode. The magnetic contrast of the skyrmions was determined from a set of three images with under-, over-, and in-focus. Samples were prepared by using focused ion beam (FIB) and the corresponding orientation was determined by selected-area electron diffraction (SAED).

Electrical transport and magnetization measurements

The magnetization and transport properties were determined using a physical property measuring system (PPMS, Quantum Design). The electrical properties were measured by standard six-probe method with J_c flowing in the [100] direction. The Hall resistivity is given by $\rho_{xy}^\perp = R_0^\perp \mu_0 H_0 + R_s^\perp \mu_0 M_z + P_z^\perp(H_0) R_0^\perp b^z$. $R_0^\perp$ and $R_s^\perp$ are the OHE and AHE coefficients, respectively. The third term is the THE resistivity ρ_{xy}^{THE} in which $P_z^\perp(H_0)$ is the net $\hat{z}$ spin polarization of the charge carriers for an OOP $\vec{H}$. M_z was measured using a VSM.

Reporting summary

Further information on research design is available in the Nature Portfolio Reporting Summary linked to this article.

Data availability

The data that support the findings of this study are available from the corresponding author upon request.

Code availability

The codes used in theoretical calculations are available from the corresponding author upon request.

References

1. Leonov, A. O. & Mostovoy, M. Multiply periodic states and isolated skyrmions in an anisotropic frustrated magnet. *Nat. Commun.* **6**, 8275 (2015).
2. Leonov, A. O. & Mostovoy, M. Edge states and skyrmion dynamics in nanostripes of frustrated magnets. *Nat. Commun.* **8**, 14394 (2017).
3. Zhang, X. et al. Skyrmion dynamics in a frustrated ferromagnetic film and current-induced helicity locking-unlocking transition. *Nat. Commun.* **8**, 1717 (2017).
4. Hayami, S. & Motome, Y. N'eel- and Bloch-type magnetic vortices in Rashba metals. *Phys. Rev. Lett.* **121**, 137202 (2018).
5. Hou, Z. et al. Observation of various and spontaneous magnetic skyrmionic bubbles at room temperature in a frustrated kagome magnet with uniaxial magnetic anisotropy. *Adv. Mater.* **29**, 1701144 (2017).
6. Hou, Z. et al. Creation of single chain of nanoscale skyrmion bubbles with record-high temperature stability in a geometrically confined nanostripe. *Nano Lett.* **18**, 1274 (2018).
7. Hou, Z. et al. Current-induced helicity reversal of a single skyrmionic bubble chain in a nanostructured frustrated magnet. *Adv. Mater.* **32**, 1904815 (2020).
8. Tang, J. et al. Target Bubbles in Fe_3Sn_2 nanodisks at zero magnetic field. *ACS Nano* **14**, 10986 (2020).
9. Li, H. et al. Large topological Hall effect in a geometrically frustrated kagome magnet Fe_3Sn_2. *Appl. Phys. Lett.* **114**, 192408 (2019).
10. Du, Q. et al. Topological Hall Effect Anisotropy in Kagome Bilayer Metal Fe_3Sn_2. *Phys. Rev. Lett.* **129**, 236601 (2022).
11. Kida, T. et al. The giant anomalous Hall effect in the ferromagnet Fe_3Sn_2—a frustrated kagome metal. *J. Phys.: Condens. Matter* **23**, 112205 (2011).
12. Ye, L. et al. Massive Dirac fermions in a ferromagnetic kagome metal. *Nature* **555**, 638 (2018).
13. Wei, W. et al. Current-controlled topological magnetic transformations in a nanostructured kagome magnet. *Adv. Mater.* **33**, 2101610 (2021).
14. Jiang, J. et al. Current-controlled skyrmion number in confined ferromagnetic nanostripes. *Adv. Funct. Mater.* **33**, 2304044 (2023).
15. Jonietz, F. et al. Spin transfer torques in MnSi at ultralow current densities. *Science* **330**, 1648 (2010).
16. Murakami, S., Nagaosa, N. & Zhang, S.-C. Dissipationless quantum spin current at room temperature. *Science* **301**, 1348 (2003).
17. Sinova, J. et al. Universal intrinsic spin hall effect. *Phys. Rev. Lett.* **92**, 126603 (2004).
18. Šmejkal, L., Mokrousov, Y., Yan, B. & MacDonald, A. H. Publisher correction: topological antiferromagnetic spintronics. *Nat. Phys.* **14**, 766 (2018).
19. Ohgushi, K., Murakami, S. & Nagaosa, N. Spin anisotropy and quantum Hall effect in the kagome lattice: Chiral spin state based on a ferromagnet. *Phys. Rev. B* **62**, R6065 (2000).
20. Taguchi, Y., Oohara, Y., Yoshizawa, H., Nagaosa, N. & Tokura, Y. Spin chirality, Berry phase, and anomalous Hall Effect in a frustrated ferromagnet. *Science* **291**, 2573 (2001).
21. Bruno, P., Dugaev, V. K. & Taillefumier, M. Topological Hall Effect and Berry phase in magnetic nanostructures. *Phys. Rev. Lett.* **93**, 096806 (2004).
22. Yin, G., Liu, Y., Barlas, Y., Zang, J. & Lake, R. K. Topological spin Hall effect resulting from magnetic skyrmions. *Phys. Rev. B* **92**, 024411 (2015).
23. Denisov, K. S., Rozhansky, I. V., Averkiev, N. S. & Lähderanta, E. General theory of the topological Hall effect in systems with chiral spin textures. *Phys. Rev. B* **98**, 195439 (2018).
24. Rozhansky, I. V., Denisov, K. S., Lifshits, M. B., Averkiev, N. S. & Lähderanta, E. Topological and Chiral Spin Hall effects. *Phys. Status Solidi (b)* **256**, 1900033 (2019).
25. Buhl, P. M., Freimuth, F., Blügel, S. & Mokrousov, Y. Topological spin Hall effect in antiferromagnetic skyrmions. *Phys. Status Solidi (RRL) – Rapid Res. Lett.* **11**, 1700007 (2017).
26. Akosa, C. A., Tretiakov, O. A., Tatara, G. & Manchon, A. Theory of the topological spin hall effect in antiferromagnetic skyrmions: impact on current-induced motion. *Phys. Rev. Lett.* **121**, 097204 (2018).
27. Mochizuki, M. Spin-wave modes and their intense excitation effects in skyrmion crystals. *Phys. Rev. Lett.* **108**, 017601 (2012).
28. Onose, Y., Okamura, Y., Seki, S., Ishiwata, S. & Tokura, Y. Observation of magnetic excitations of skyrmion crystal in a helimagnetic insulator Cu_2OSeO_3. *Phys. Rev. Lett.* **109**, 037603 (2012).
29. Schwarze, T. et al. Universal helimagnon and skyrmion excitations in metallic, semiconducting and insulating chiral magnets. *Nat. Mater.* **14**, 478 (2015).
30. Ehlers, D. et al. Skyrmion dynamics under uniaxial anisotropy. *Phys. Rev. B* **94**, 014406 (2016).
31. Satywali, B. et al. Microwave resonances of magnetic skyrmions in thin film multilayers. *Nat. Commun.* **12**, 1909 (2021).
32. Srivastava, T. et al. Resonant dynamics of three-dimensional skyrmionic textures in thin film multilayers. *APL Mater.* **11**, 061110 (2023).
33. Liu, L., Moriyama, T., Ralph, D. C. & Buhrman, R. A. Spin-Torque ferromagnetic resonance induced by the Spin Hall effect. *Phys. Rev. Lett.* **106**, 036601 (2011).
34. Giefers, H. & Nicol, M. High pressure X-ray diffraction study of all Fe–Sn intermetallic compounds and one Fe–Sn solid solution. *J. Alloy. Compd.* **422**, 132 (2006).

35. Capua, A. et al. Phase-resolved detection of the spin Hall angle by optical ferromagnetic resonance in perpendicularly magnetized thin films. *Phys. Rev. B* **95**, 064401 (2017).

36. Grover, B. et al. Crystallographic dependence of the spin Hall angle in epitaxial Pt films: comparison of optical and electrical detection of spin-torque ferromagnetic resonance techniques. *Appl. Phys. Lett.* **120**, 172406 (2022).

37. Khan, K. I. A. et al. Magnetodynamic properties of ultrathin films of Fe_3Sn_2 a topological kagome ferromagnet. *Sci. Rep.* **14**, 3487 (2024).

38. Neubauer, A. et al. Topological Hall Effect in the A-Phase of MnSi. *Phys. Rev. Lett.* **102**, 186602 (2009).

39. Raju, M. et al. The evolution of skyrmions in Ir/Fe/Co/Pt multilayers and their topological Hall signature. *Nat. Commun.* **10**, 696 (2019).

40. Wang, H., Dai, Y., Chow, G.-M. & Chen, J. Topological hall transport: Materials, mechanisms and potential applications. *Prog. Mater. Sci.* **130**, 100971 (2022).

41. Jiang, N., An, H., Bai, Y., Yang, B. & Zhao, S. Planar Hall effect modified by the evolution of magnetic domain states. *J. Phys. Chem. C.* **127**, 9154 (2023).

42. Denisov, K. S., Rozhansky, I. V., Averkiev, N. S. & Lähderanta, E. A nontrivial crossover in topological Hall effect regimes. *Sci. Rep.* **7**, 17204 (2017).

43. Tao, Y., Daemen, L., Cheng, Y., Neuefeind, J. C. & Louca, D. Investigating the magnetoelastic properties in FeSn and Fe_3Sn_2 flat band metals. *Phys. Rev. B* **107**, 174407 (2023).

44. Lin, Z.-Z. & Chen, X. Tunable massive Dirac fermions in ferromagnetic Fe_3Sn_2 Kagome Lattice. *Phys. status solidi (RRL) – Rapid Res. Lett.* **14**, 1900705 (2020).

45. Donahue, M.J. & Porter, D. G. *The Object Oriented MicroMagnetic Framework (OOMMF) program*, NISTIR, (1999).

46. Zhang, S. & Li, Z. Roles of nonequilibrium conduction electrons on the magnetization dynamics of ferromagnets. *Phys. Rev. Lett.* **93**, 127204 (2004).

47. Hou, Z. et al. Current-induced reversible split of elliptically distorted skyrmions in geometrically confined Fe_3Sn_2 Nanotrack. *Adv. Sci.* **10**, 2206106 (2023).

48. Zahnd, G. et al. Spin diffusion length and polarization of ferromagnetic metals measured by the spin-absorption technique in lateral spin valves. *Phys. Rev. B* **98**, 174414 (2018).

Author contributions
N.B., W.W., and A.C. conceived the research. Y.C.L., W.W., I.R., and A.C. supervised the experiments. H.L., Y.C.L., and W.W. fabricated and characterized the sample. N.B. performed the dynamical measurements. N.B. and B.A. performed the simulations. H.L. performed the transport measurements and the LTEM imaging. All authors discussed the results and co-wrote the manuscript. A.C. and W.W. directed the research.

Competing interests
The authors declare no competing interests.

Additional information
Supplementary information The online version contains supplementary material available at https://doi.org/10.1038/s41467-025-59899-5.

Correspondence and requests for materials should be addressed to Amir Capua.

Peer review information *Nature Communications* thanks Masahito Mochizuki, and the other, anonymous, reviewer(s) for their contribution to the peer review of this work. A peer review file is available.

Reprints and permissions information is available at http://www.nature.com/reprints

Publisher's note Springer Nature remains neutral with regard to jurisdictional claims in published maps and institutional affiliations.